Journal of the Brazilian Society of Mechanical Sciences and Engineering (2020) 42:537
https://doi.org/10.1007/s40430-020-02628-4

TECHNICAL PAPER

Experimental investigation on mechanical behaviors of Q345B steel material over wide ranges of strain rates and temperatures

Tao Jiang[1] · Chong Ji[1] · Xin Wang[1] · Ying Liu[1] · Changxiao Zhao[1] · Yuxiang Sun[1] · Kun Zhang[1]

Received: 20 May 2020 / Accepted: 15 September 2020 / Published online: 24 September 2020

Abstract
In the present study, the stress–strain relationships of Q345B steel with the coupling effect of temperature and strain rate were primarily investigated. First, the quasi-static tensile test and dynamic impact compression test were performed using the 810 material test system and the split Hopkinson pressure bar device, respectively, at temperatures ranging from 25 to 700 °C and the strain rate ranging from 0.001 to 4000 s^{-1}. Second, thermal and strain-rate effects on the mechanical behavior of Q345B steel material steel were studied. It was reported that Q345B steel can be significantly softened with temperatures and hardened with strain rates. Finally, a modified Johnson–Cook (J–C) model was developed to describe the nonlinear mechanical behavior of Q345B steel material over a wide range of strain rates and temperatures.

Keywords Q345B steel · Split Hopkinson pressure bar · High temperature · High strain rate · Johnson–Cook constitutive equation

1 Introduction

As a comprehensive mechanical and building material, low-alloy Q345B steel is extensively used in bridges, buildings, pressure vessels, and special equipment, among other fields. It is possible for engineering structures to be exposed to extreme dynamic loads during their service life, such as industrial explosion accidents, bomb explosions, fire, and accidental collisions [1–5]. To accurately design and evaluate the performance of engineering structures under such extreme dynamic loads, it is necessary to study the mechanical behavior of the material, especially the dynamic mechanical properties.

It has been experimentally proven that the properties of materials generally differ between dynamic and static states. The dynamic mechanical properties of a material are known to be dependent on the strain, strain rate, and temperature. The split Hopkinson pressure bar (SHPB) device has become an effective experimental technique to study the dynamic behavior of materials over a wide range of strain rates [6–9]. The specially modified SHPB system can be used to investigate material properties at different temperatures.

Numerous experimental studies on the dynamic behavior of materials such as metals have been conducted by many researchers. Whittington et al. [10] investigated the mechanical response and damage evolution of RHA steel. High strain-rate experiments conducted via SHPB showed increased strength and reduced failure strains. An internal state variable (ISV) plasticity/damage model was used to capture the varying effects of temperature, strain rate, and stress state for the RHA steel with a single set of plasticity and damage parameters. Visser et al. [11] conducted research on the dynamic compressive stress–strain curve properties of low carbon steel in the range 293–923 K and at strain rates of 1000–5000 s^{-1} using SHPB. The resulting stress–strain curves were partitioned into thermal and athermal stress components in which the role of twin boundaries was discussed in terms of their relationship with the interaction of dislocation motion and grain subdivision.

An experimental study carried out by Jing [12] indicated that the D1 steel displays obvious temperature dependence, and the third type strain aging (third SA) occurred at the temperature region 673–973 K and at a strain rate of ~ 1500 s^{-1}. Li et al. [13] reported slow-, intermediate-, and high-strain-rate experiments that were carried out on DP800

Technical Editor: João Marciano Laredo dos Reis.

✉ Chong Ji
2468645816@qq.com

[1] College of Field Engineering, Army Engineering University of PLA, Nanjing 210007, China

steel specimens using the SHPB testing system with the load inversion device. The experimental results revealed a non-monotonic effect of the temperature on the stress–strain curve for DP800 steel. Niu et al. [14] investigated the dynamic compressive mechanical properties of 30CrMnSiNi2A steel at 30–700 °C and 3.0×10^3–10.0×10^3 s^{-1}. They found that 30CrMnSiNi2A has evident temperature sensitivity at 300 °C. Moreover, the flow stress significantly decreased and the strain-rate-hardening effect is obvious with the increase in temperature. In addition to the above, Lee et al. [15] utilized SHPB to compare the impact plastic behavior of three steels (S15C carbon steel, S50C medium alloy steel, and SKS93 tool steel) under strain rates ranging from 1.1×10^3 to 5.5×10^3 s^{-1} and temperatures ranging from 25 to 800 °C. The effects of the carbon content, strain rate, and temperature on the mechanical responses of steels were evaluated.

Johnson–Cook (J–C) constitutive equations have been widely used to describe the dynamic mechanical behavior of metallic materials. Therefore, many researchers have established or modified J–C models of some materials through quasi-static and SHPB experiments. The characterization of Armox 500T steel investigated by Iqbal [16] showed an increase in strength with the increase in stress triaxiality as well as strain rate. The results thus obtained from experiments on the specimens of both the materials were subsequently employed for calibrating the material parameters of the J–C model. Erice et al. [17] investigated the flow and fracture behavior of FV535 martensitic stainless steel at different strain rates and temperatures. Experimental data are matched using ABAQUS/Standard and LS-DYNA numerical codes. This method allows the researcher to obtain critical data of equivalent plastic strain and triaxility, which allows for a more precise calibration of the J–C model. Brown et al. [18] presented new J–C parameters for the AK47 steel core by SHPB compression testing. Effects of strain-rate and temperature for the titanium alloy (Ti–6Al–4V) were investigated by Seo [19]. The parameters for a modified J–C constitutive equation were determined from the test results.

In recent years, researchers have studied the mechanical properties of other materials, such as A533B steel [20], 42CrMo steel [21], TWIP steel [22], 603 steel [23], 316L stainless steel [24, 25], beryllium copper [26], Ti–6Al–4V alloy [27], Ti–6.6Al–3.3Mo–1.8Zr–0.29Si alloy [28], aluminum alloys [29, 30], and Al–Mg–Si alloy [31] by quasi-static and SHPB tests under different strain rates and temperatures. However, there is a lack of investigation on the dynamic mechanical properties of Q345B steel under different strain rates and ambient temperatures, and there is no suitable constitutive model to describe the dynamic mechanical properties of Q345B steel material.

In this study, the stress–strain relationships of Q345B steel with the coupling effect of strain rate and temperature were primarily investigated. Quasi-static tensile and compression tests of Q345B steel at 0.035 s^{-1} strain rate and the temperature ranging from 25 to 700 °C were conducted using the MTS810 and MTS809 material test system. Dynamic compression experiments at temperatures ranging from 25 to 700 °C and the strain rates ranging from 500 to 4000 s^{-1} were performed using the ALT1000 SHPB setup. The thermal and strain-rate effects are discussed. A modified J–C model was developed to describe the nonlinear mechanical behavior of Q345B steel material over a wide range of strain rates and temperatures.

2 Quasi-static tensile and compression tests

2.1 Test device and methods

Quasi-static tensile experiments were performed on Q345B steel specimens at different temperatures to obtain the stress–strain curves, yield strength, and other vital parameters. MTS810 and MTS809 microcomputer control electronic testing machines were adopted as the test equipment for quasi-static tensile tests. For the particularity of high-temperature experiment, the tests were divided into two groups in accordance with the temperature range: *A* and *B*.

Group *A* was the tensile test under temperatures ranging from 25 to 500 °C. The MTS810 material testing system was adopted as the test equipment, as shown in Fig. 1a. MTS810 test machine was adopted to load at a deformation rate of 0.035 mm s^{-1} with high-temperature extensometer used to accurately measure strain changes. The electric heating furnace, namely, 651 Environmental Chamber, was employed to heat the specimen and clamping parts simultaneously at a temperature rise rate of 20 °C min^{-1}. After the specified temperature was reached, the time of heat preservation was supposed to be at least 20 min before loading. To detect the temperature of the heating furnace and the specimen, the matching FLUKE54 II B thermometer and thermocouple was adopted, as shown in Fig. 1b. The test at each temperature was repeated thrice, and the average value was used.

Group *B* was the tensile test under temperatures of 600–700 °C. MTS810 material testing system, as shown in Fig. 2a, was employed for loading at the identical deformation rate with the same extensometer. MTS653 furnace was used to heat the specimen at the identical temperature rise rate and simultaneously maintain warmth. Similar thermometer and thermocouple were used. However, the difference was that there were two heating units in the furnace (as shown in Fig. 2b), and it could only heat the parallel length of the specimen, probably leading to a certain temperature gradient on the surface of the specimen. To eliminate the

(a) 810 Material test system. **(b)** Thermocouple and thermometer.

Fig. 1 Experimental apparatus at the temperature range of 25–500 °C. **a** 810 material test system. **b** Thermocouple and thermometer

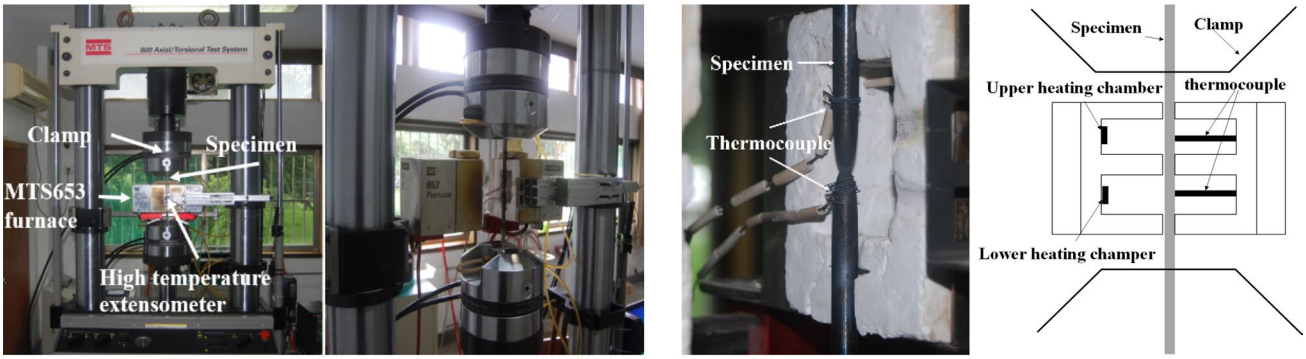

(a) 809 Axial/Torsional Test System. **(b)** Layout of furnace heating.

Fig. 2 Experimental apparatus at the temperature range of 600–700 °C. **a** 809 axial/torsional test system. **b** Layout of furnace heating

effect of temperature gradient, two thermocouples, as shown in Fig. 2b, whose ends were wound with copper wire to the part closest to the middle of the specimen, were used to detect the temperature of the specimen. If the thermometer presented a temperature gradient on the specimen, the temperature gradient could be regulated within 0.5 °C by adjusting the heating units. The test at each temperature was also repeated thrice and the average value was used.

The quasi-static compression test was also carried out on the MTS810 material testing system using the same high-temperature extensometer and thermometer. However, the clamp was replaced according to the shape of the specimen, as shown in Fig. 3. Due to the limitation of experimental equipment performance, the maximum temperature of high-temperature compression test was only 500 °C.

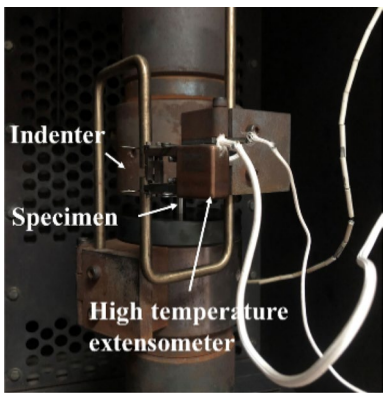

Fig. 3 Installation diagram of high-temperature compression test

2.2 Test specimens

Low-alloy Q345B steel was used in this study. Table 1 gives the chemical composition of Q345B steel. The coupon test specimens were taken from the same batch steel ingot. The specimens of different sizes were processed according to the different high-temperature test equipment. The quasi-static tensile test specimens were prepared in accordance with the Chinese standard GB/T 228.1-2010 [32] and GB/T 228.2-2015 [33], while the quasi-static compression test

Table 1 Chemical composition of Q345B steel (%)

C	Si	Mn	P	S	Ti	V	Ni	Cr	Cu	Al	Fe
0.17	0.44	0.14	0.02	0.01	0.01	–	0.01	0.04	0.01	0.018	Bal.

specimens were processed according to GB/T 7314-2017 [34]. The dimensions and physical drawing of the specimens are shown in Fig. 4.

2.3 Results and analysis

The morphology of the specimens after tensile and compression is shown in (b) compressed specimen.

In Figure 5, It can be clearly seen that the color of the tensile fracture specimen and the compression specimen significantly changed at 300 °C, and both were blue. Table 2 shows the percentage elongation after fracture (A) and percentage reduction of area (Z) of the tensile specimen at different temperatures. The data in Table 2 illustrate that A and Z show a decreasing trend after fracture within 300 °C. When the temperature is not less than 300 °C, A and Z begin to gradually increase with the rise in temperature. It is initially speculated that some steels have the phenomenon of "blue brittle" in a certain temperature range, in which the steel will appear dark blue, and the plasticity of materials decreases while brittleness increases.

Through equation transformation, the true stress–strain curve at a quasi-static state is obtained, as shown in Fig. 6. As can be seen from the figure above, unlike the tensile curve, the compression curve continues to rise because Q345B steel as a plastic material can only deform but not break when compressed. It indicates that the stress/strain state has a certain influence on the shape of the curve [35]. The tensile and compressive stress–strain curves show the obvious softening effect due to the temperature: the flow stress basically decreased with the rise in temperature. However, stress did not strictly decrease with temperature. When the temperature was in the range of 100–300 °C, the flow stress increased with temperature, showing a temperature hardening effect. The reason for these could be explained by "blue brittle": When the temperature rose to a certain temperature range (blue brittleness temperature), the diffusion speed of C and N atoms rapidly increased, keeping abreast with the slip speed of the dislocation. Repeated pinning–depinning–pinning of C and N atoms on the dislocation occurs, thus showing an increase in deformation resistance on the macro-level [36]. The tensile and compressive stress–strain curves both have an obvious yield platform within 300 °C. When the temperature exceeds 300 °C, the yield platform gradually disappears. In addition, there are oscillations in both stress–strain curves of 200 °C, which is due to the involvement of the twining deformation. At 200 °C, the twining strain rate exceeds the movement speed of the testing machine clamp, leading to local stress relaxation and serrated appearance on the curve [37].

Table 3 shows the yield strength (f_y) of Q345B steel at different temperatures under tensile and compression tests. Tables 4 and 5 illustrate the tensile strength (R_m) and elastic modulus (E) at different temperatures under tensile tests. Due to the particularity of the compression curve of plastic material and the inhomogeneous deformation of the compression specimen during compression loading, the compression strength and elastic modulus of the specimen at different temperatures are not provided. The data in Table 3 revealed that the yield strength values of the specimens at the same temperature under tensile and compression tests were consistent, and the yield strength fitting curves of the two were also very close, as shown in Fig. 7a. It indicates that the yield strength of Q345B steel is isotropic in tensile and compression tests. In addition, f_y and E of Q345B steel basically decreased with the rise in temperature during tensile tests, while R_m first decreased, then increased, and then decreased again. By the mathematical regression analysis of three mechanical properties at different temperatures (as shown in Fig. 7), the regression equations were obtained (Eqs. 1–3) with the correlation coefficients R^2 being 0.9681, 0.9904, and 0.9949, respectively, which could well reflect the changes in yield strength, tensile strength, and elastic modulus with temperature, respectively.

$$f_y(T) = -0.3824T + 382.39\,(\text{MPa}), \tag{1}$$

$$R_m(T) = 2.3 \times 10^{-8}T^4 - 3.27 \times 10^{-5}T^3 + 0.013T^2 - 1.54T + 573.2\,(\text{MPa}), \tag{2}$$

$$E(T) = 1.9 \times 10^{-9}T^4 - 2.74 \times 10^{-6}T^3 + 1.02 \times 10^{-3}T^2 - 0.156T + 209.5\,(\text{GPa}). \tag{3}$$

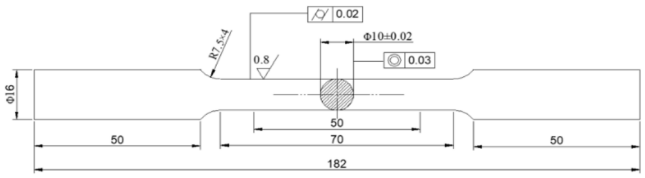

(a) Dimensions of tensile specimen in Group A (mm).

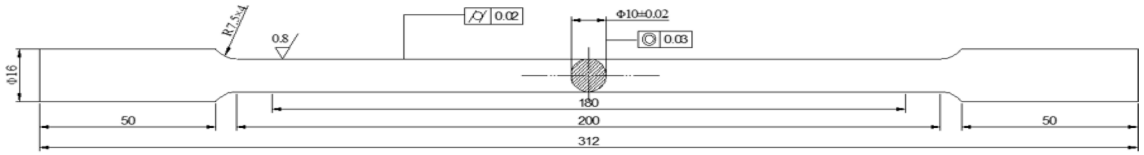

(b) Dimensions of tensile specimen in Group B (mm).

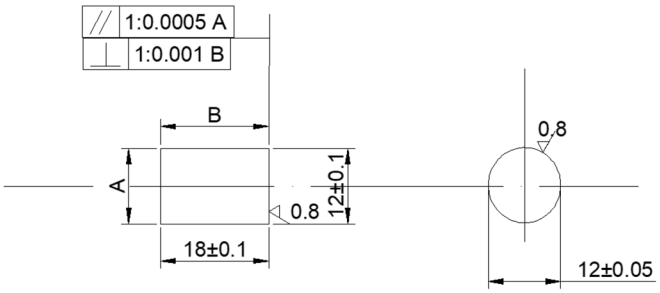

(c) Dimensions of compression specimen (mm).

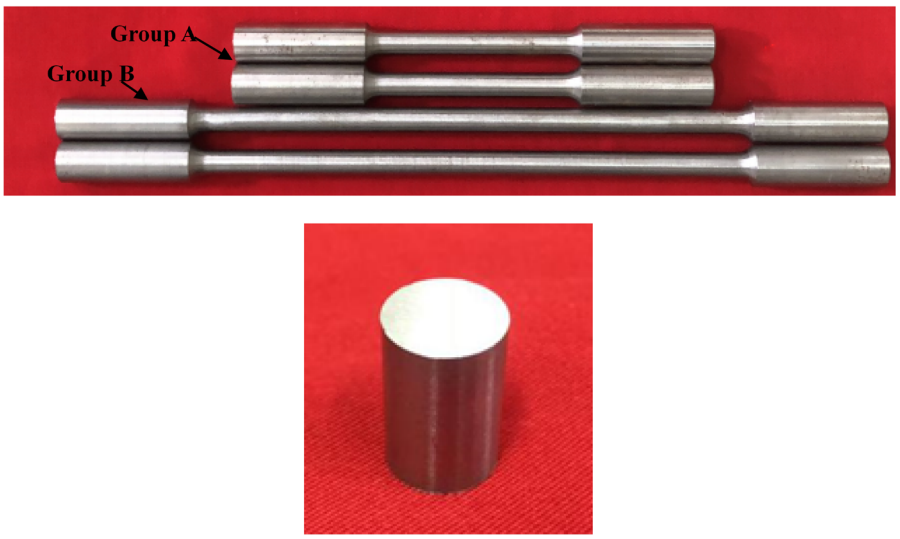

(d) Physical drawing of the specimens.

Fig. 4 Specimens of tensile and compression tests. **a** Dimensions of tensile specimen in group A (mm). **b** Dimensions of tensile specimen in group B (mm). **c** Dimensions of compression specimen (mm). **d** Physical drawing of the specimens

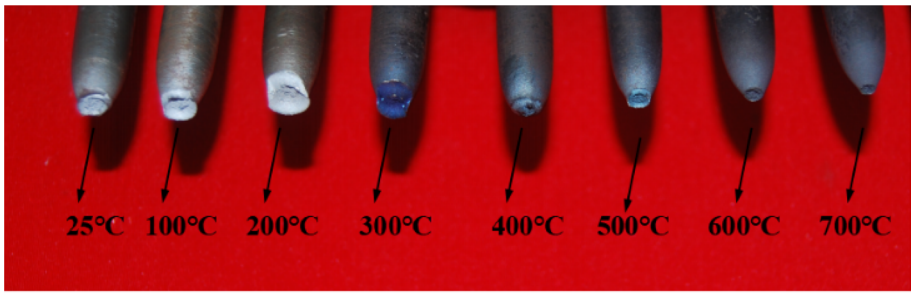

(a) Tensile fracture specimen.

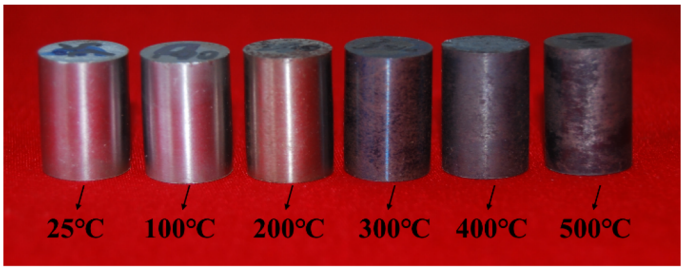

(b) Compressed specimen.

Fig. 5 Appearance of the specimen after experiment. **a** Tensile fracture specimen. **b** Compressed specimen

Table 2 Percentage elongation after fracture (A) and percentage reduction of area (Z) of the tensile specimen

Temperature (°C)	25	100	200	300	400	500
A (%)	37	34.1	35.6	38.8	43.1	51.9
Z (%)	49	47	39	49	59	66

3 SHPB dynamic compression experiments and results

3.1 SHPB apparatus and experimental techniques

The SHPB apparatus has been extensively used to test the dynamic mechanical behavior of various engineering materials. Figure 8 shows the schematic diagram of the high-temperature SHPB apparatus used in this paper. A striker bar controlled by a gas gun impacts the end of the incident bar, generating a compressive stress wave (the incident pulse ε_i) on the incident bar. When the incident bar comes in contact with the specimen, the stress wave also reaches the specimen. Afterward, a reflected wave (the reflected pulse ε_r) reflects to the incident bar, and a transmitted wave (the transmission pulse ε_t) continues to travel along the transmission bar. Strain gauges are adopted to record strain pulse, and the stress–strain data of the specimen under dynamic effect are harvested by calculating the following relations:

$$\dot{\varepsilon}(t) = \frac{C_0}{L}\left[\varepsilon_i(t) - \varepsilon_r(t) - \varepsilon_t(t)\right], \tag{4}$$

$$\varepsilon(t) = \frac{C_0}{L}\int_0^t \left[\varepsilon_i(t) - \varepsilon_r(t) - \varepsilon_t(t)\right]\mathrm{d}t, \tag{5}$$

$$\sigma(t) = \frac{EA}{2A_0}\left[\varepsilon_i(t) + \varepsilon_r(t) + \varepsilon_t(t)\right], \tag{6}$$

where $\dot{\varepsilon}(t)$, $\varepsilon(t)$, $\sigma(t)$, C_0, A, E, A_0, and L denote the strain-rate, strain, flow stress, wave velocity in the bars, cross-sectional area and elastic modulus of the bars, cross-sectional area, and the original length of the specimen, respectively. Subsequently, the stress–strain curve of the material can be obtained by calculation.

The compressive SHPB system for high-temperature tests also includes a heating and temperature control system, as shown in Fig. 9. In this paper, a type of high-temperature SHPB system, ALT1000 device, is adopted, as shown in Fig. 9a. Before the experiment, the cylindrical specimen

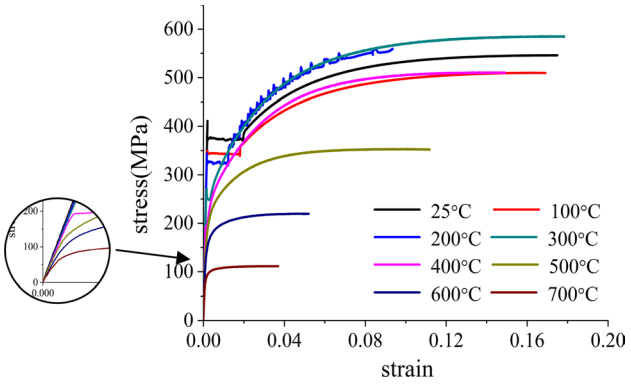

(a) Tensile stress-strain curve.

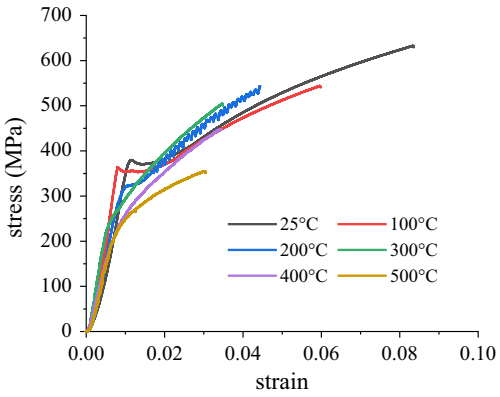

(b) Compression stress-strain curve.

Fig. 6 True stress–strain curves at different temperatures for quasi-static experiments. **a** Tensile stress–strain curve. **b** Compression stress–strain curve

($\phi 8 \times 5$ mm) was first fixed at the end of the incident bar. To avoid the influence of temperature on the two bars, a sleeve was designed so that the specimen can be independently heated, as shown in Fig. 9e. Then, the high-temperature thermocouple (Fig. 9f) was fixed on the surface of the specimen to measure the temperature. After the specimen was pushed into the heating furnace (Fig. 9b) for heating, the PID temperature controller, as shown in Fig. 9c, was adopted to regulate the temperature, for which the precision was within ± 1 °C. After the specimen was heated to the required temperature and was maintained for 20 min, the impact test can be performed. In the SHPB test, strain rate was controlled by the speed of the striker bar, such that the velocity of striker bar under specified strain rate was measured by a speedometer (Fig. 9h) before the experiment. Finally, the waveform data were harvested through strain gauges pasted at specified positions on the input and output bar, as shown in Fig. 9g. The stress–strain data were obtained through the data acquisition and processing system.

3.2 Results and analysis

Figure 10 presents the true stress–strain relationships of Q345B steel at different temperatures for various strain rates. In the dynamic tests, the material also displayed an obvious softening effect. But the strength increased when the temperature reached 500 °C, which can also be explained by "blue brittle." However, unlike quasi-static, it happened at higher temperatures. According to the theory of dislocation dynamics, the initial temperature of blue brittle increases with the rise in strain rate [36]. In addition, under the condition of dynamic strain rate, the curve still had obvious yield platform when the temperature exceeded 300 °C.

The flow stress–temperature relationship at strains of 0.04, 0.08, 0.12, 0.16, and 0.20 for the strain rate of 2000 s^{-1} is presented in Fig. 11. The difference in flow stress between adjacent strains roughly decreases as the temperature increases, indicating that the work-hardening

Table 3 Yield strength of Q345B steel at different temperatures (MPa)

T (°C)	25	100	200	300	400	500	600	700	800
Compression tests (f_y)	370.3	353.1	324	272	212	198	–	–	–
Tensile tests (f_y)	370.7	338.8	324.4	247.8	224.7	206.6	169.7	96.1	56.1

Table 4 Tensile strength of Q345B steel at different temperatures (MPa)

T (°C)	25	100	200	300	400	500	600	700
Tensile strength (R_m)	546.1	510	553.9	585.2	510.4	352.4	219.8	111.2

Table 5 Elastic modulus of Q345B steel at different temperatures (GPa)

T (°C)	25	100	200	300	400	500	600	700
Elastic modulus (E)	206	201.7	201.7	193.6	186.1	166.1	140.3	124

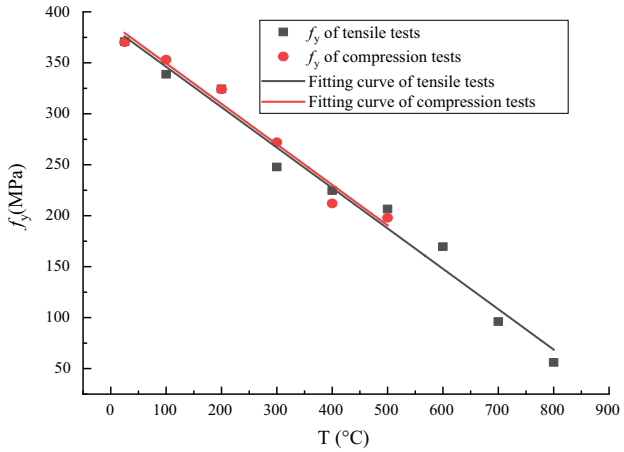

(a) Yield strength fitting curve.

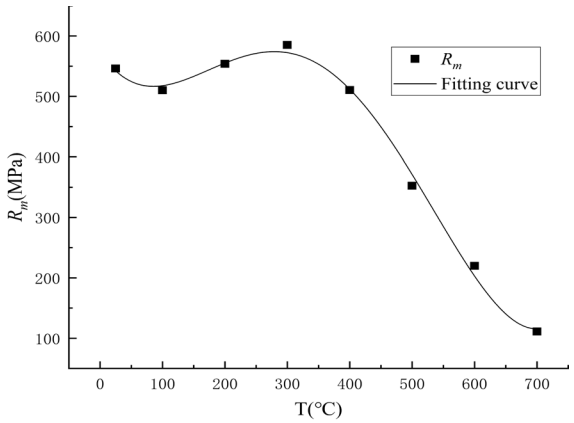

(b) Tensile strength fitting curve.

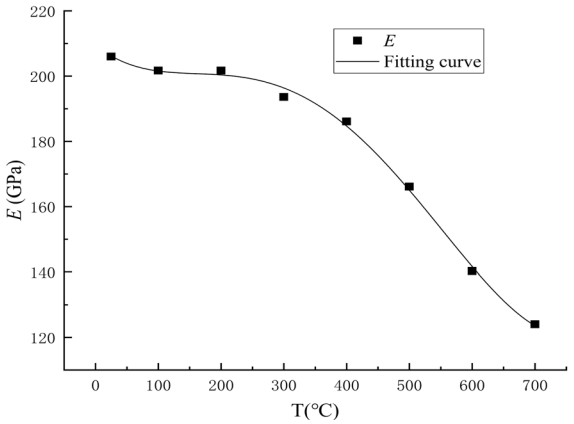

(c) Elastic modulus fitting curve under tensile tests.

Fig. 7 f_y, R_m, E fitting curves at different temperatures. **a** Yield strength fitting curve. **b** Tensile strength fitting curve. **c** Elastic modulus fitting curve under tensile tests

effect decreases continuously with the rise in temperature. According to the varying trend of stress at a given strain, the flow stress quickly decreases when the temperature is beyond 300 °C. In other words, thermal softening effect at temperatures higher than 300 °C seems more obvious than below 300 °C.

To elucidate the effect of strain rate on the mechanical behavior of Q345B steel, stress–strain curves of dynamic compression and quasi-static compression at various temperatures are plotted in Fig. 12. The entire plastic hardening procedure occurs at a higher stress in the dynamic experiments than in the quasi-static experiments, proving that Q345B steel has a noticeable strain-rate-hardening effect. However, materials did not always exhibit strain-rate-hardening effects. When the strain rate exceeded 2000 s^{-1}, the material strength decreased with the rise in strain rate, displaying a strain-rate-softening effect.

The variation in yield stress with strain rate at different temperatures is shown in Fig. 13. In general, with the increase in strain rate, yield strength increased at different temperatures. However, as to the slope trend, strain-rate-hardening capacity decreased. For a given temperature, when the strain rate increased from quasi-static to 500 s^{-1}, the yield stress sharply increased. However, when the strain rate exceeded 2000 s^{-1}, the stress value changed little or even decreased with the increase in strain rate. This indicates that at a higher strain rate, Q345B steel became insensitive to the change in strain rate, and strain-rate-softening effect might occur.

4 The J–C constitutive model of Q345B steel

The J–C constitutive model synthetically contains the effect of strain, strain rate, and temperature on most metal materials. Its characteristics of simple form, clear physical meaning, and easy testability and calibration parameters aid in extensively employing it in the field of explosion and impact. Johnson and Cook [38] suggested the constitutive relation as expressed in Eq. (7):

$$\sigma=\left[A+B(\bar{\varepsilon})^{\mathrm{n}}\right]\left[1+C\ln\dot{\varepsilon}^{*}\right]\left[1-(T^{*})^{m}\right], \tag{7}$$

where σ is the flow stress; $\bar{\varepsilon}$ is the plastic strain; $\dot{\varepsilon}^{*}=\dot{\varepsilon}/\dot{\varepsilon}_0$ is the effective plastic strain rate ($\dot{\varepsilon}$ is the plastic strain rate and $\dot{\varepsilon}_0$ is the reference strain rate); and $T^{*}=(T-T_0)/(T_{\mathrm{m}}-T_0)$ is the homologous temperature (T_0 is a reference temperature, generally taken as the ambient temperature. T_{m} represents

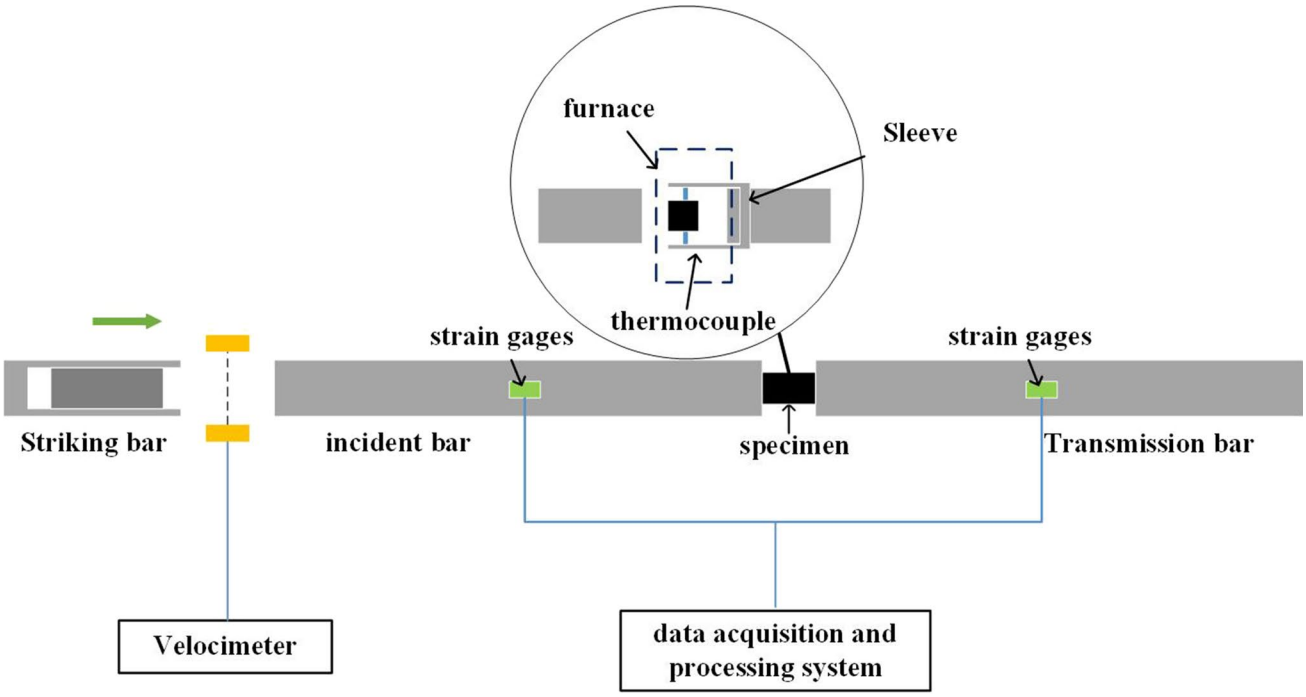

Fig. 8 Schematic diagram of the high-temperature compressive SHPB apparatus

the melting temperature). In this study, 0.001 s^{-1} is taken as the reference strain rate. The ambient temperature and melting temperature are 25 and 1500 °C, respectively. *A, B, n, C, m* are the five material constants obtained by fitting experimental data.

For the subsequent decreasing parts of the flow stress curves under dynamic strain rate, the compression test results may show increasing errors in prediction due to its work-hardening effect [35]. Therefore, *A, B,* and *n* are determined by quasi-static tensile test; *C* and *m* are calculated from the SHPB test. The five material constants for the J–C model are listed in Table 6.

4.1 Comparison between experimental data and the J–C model

A comparison between the experimental data and the J–C model of Q345B steel at high strain rates and elevated temperatures is plotted in Fig. 14. At the dynamic strain rate and temperatures below 300 °C, the results of the J–C model are nearly higher than the stress values of experimental data, while they fit relatively well at high temperatures, including the tolerance for error. Nevertheless, the opposite is true for quasi-static conditions. Under quasi-static conditions, the J–C model is consistent with the experimental data curve while slightly different at high temperatures, and the results of J–C equation are higher. This phenomenon can be explained by the following reasons.

4.2 Modification of the constitutive equation for Q345B steel

4.2.1 Adiabatic temperature rise effect

It is generally known that the SHPB test is an adiabatic process and the temperature rise during the test will impact the experimental results. When a material deforms plastically, some of the work will be converted into heat and the temperature rise during the process can further reduce the flow stress of the specimen [39]. For high-strain-rate tests, the adiabatic temperature rise is especially significant and almost negligible at quasi-static conditions. In addition, the temperature rise during the SHPB test can be calculated by the following equation [40]:

Fig. 9 Experimental equipment and setup. **a** ALT1000. **b** Heating furnace. **c** PID temperature controller. **d** Specimen. **e** Fixation of the specimen. f Fixation of thermocouple. **g** Strain gauge. **h** Speedometer sensor

$$\Delta T = \int_0^{\varepsilon} \frac{\eta}{\rho C_{\mathrm{v}}} \sigma \mathrm{d}\varepsilon, \tag{8}$$

where the parameters η, ρ, and C_{v} denote the coefficient of heat conversion, density, and specific heat, respectively (η considered as 1, and ρ, C_{v} of Q345B steel are 7850 kg m^{-3} and 460 J kg^{-1} °C, respectively).

The stress–strain curve at strain rates 2000 and 4000 s^{-1} was taken as an example. Software was used to integrate the curve area, and the adiabatic temperature rise corresponding to different temperatures was calculated according to Eq. (8). The specific values are shown in Table 7.

The data in Table 7 show that the adiabatic temperature rise is larger under higher strain rate. For some high-strain-rate tests, it can be as high as hundreds of degrees and hence cannot be neglected. In addition, the adiabatic temperature reached a maximum of nearly 50 °C at 2000 s^{-1}, while the adiabatic temperature exceeded 70 °C at 4000 s^{-1}. It may have a more significant effect on the stress–strain curve of the material at lower experimental temperatures.

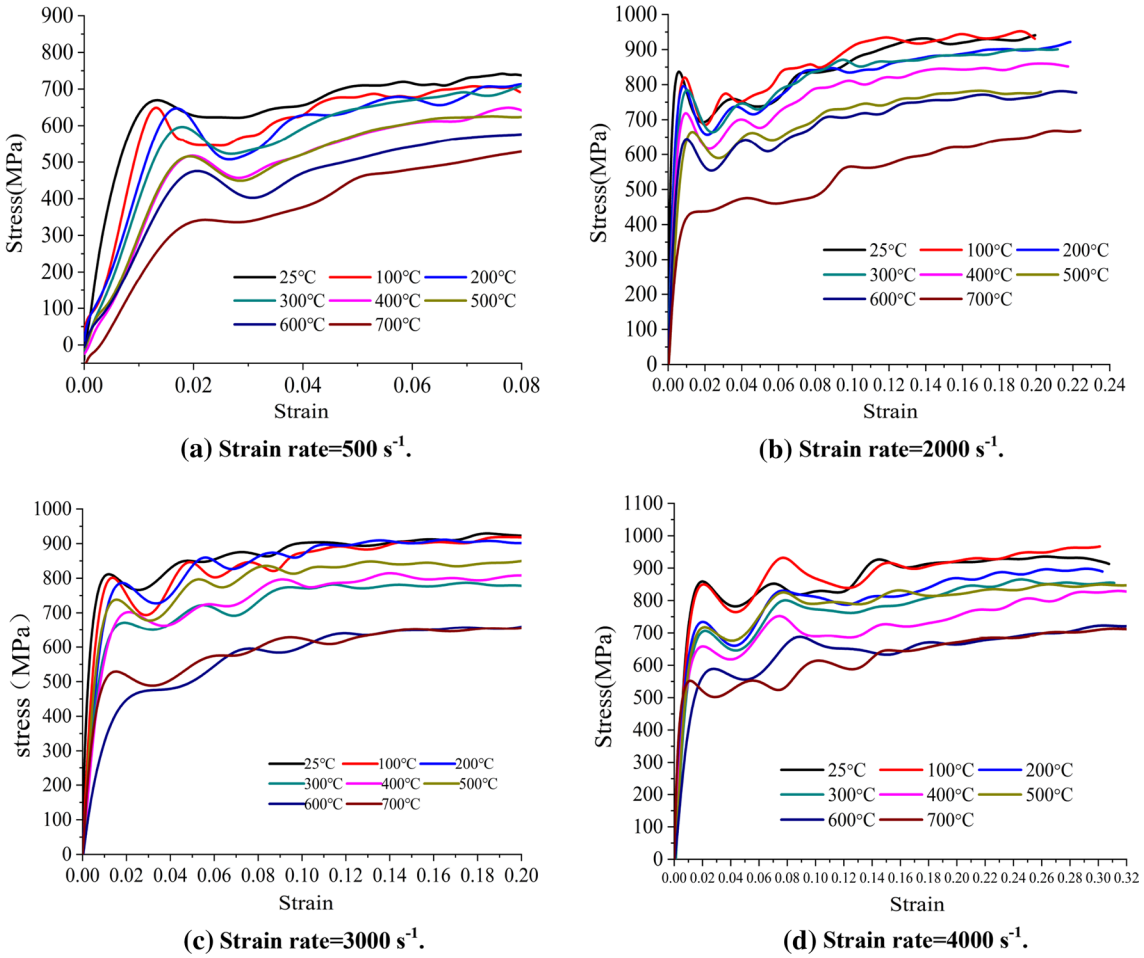

Fig. 10 True stress–strain curves at different temperatures for various strain rates. **a** Strain rate = 500 s^{-1}. **b** Strain rate = 2000 s^{-1}. **c** Strain rate = 3000 s^{-1}. **d** Strain rate = 4000 s^{-1}

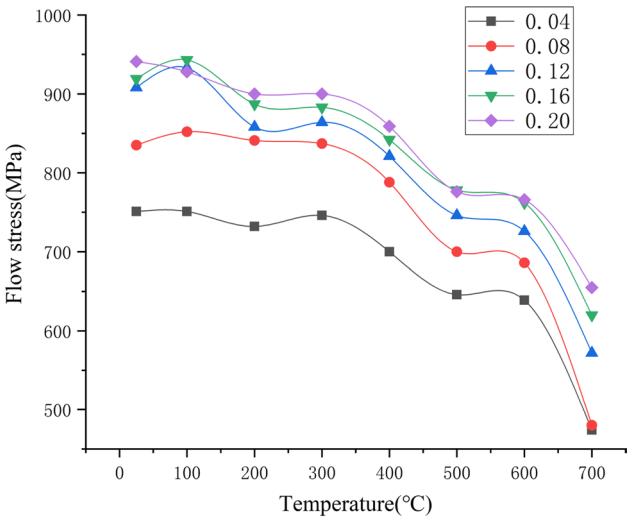

Fig. 11 Flow stress–temperature relationship at strains of 0.04, 0.08, 0.12, 0.16, and 0.20

By substituting Eq. (7) into Eq. (8) and replacing $\eta/\rho C_v$ with the parameter K, the expression of ΔT can be obtained as follows:

$$\Delta T = K(1 + C\ln\dot{\varepsilon}^*)(1 - T^{*m})\left(A\varepsilon + B\frac{\varepsilon^{n+1}}{n+1}\right). \tag{9}$$

To calculate the flow stress at adiabatic conditions using the J–C model, Sun and Guo [41] proposed an iterative calculation, and the calculation is expressed as

$$T_{i+1} = T_i + \Delta T, \tag{10}$$

$$\sigma_{i+1} = \left[A + B\left(\bar{\varepsilon}_{i+1}\right)^n\right]\left[1 + C\ln\left(\frac{\dot{\varepsilon}_{i+1}}{\dot{\varepsilon}_0}\right)\right]\left[1 - \left(T^*_{i+1}\right)^m\right]. \tag{11}$$

Then, the flow stress equation including adiabatic temperature rise effect can be obtained from Eq. (8) to Eq. (11):

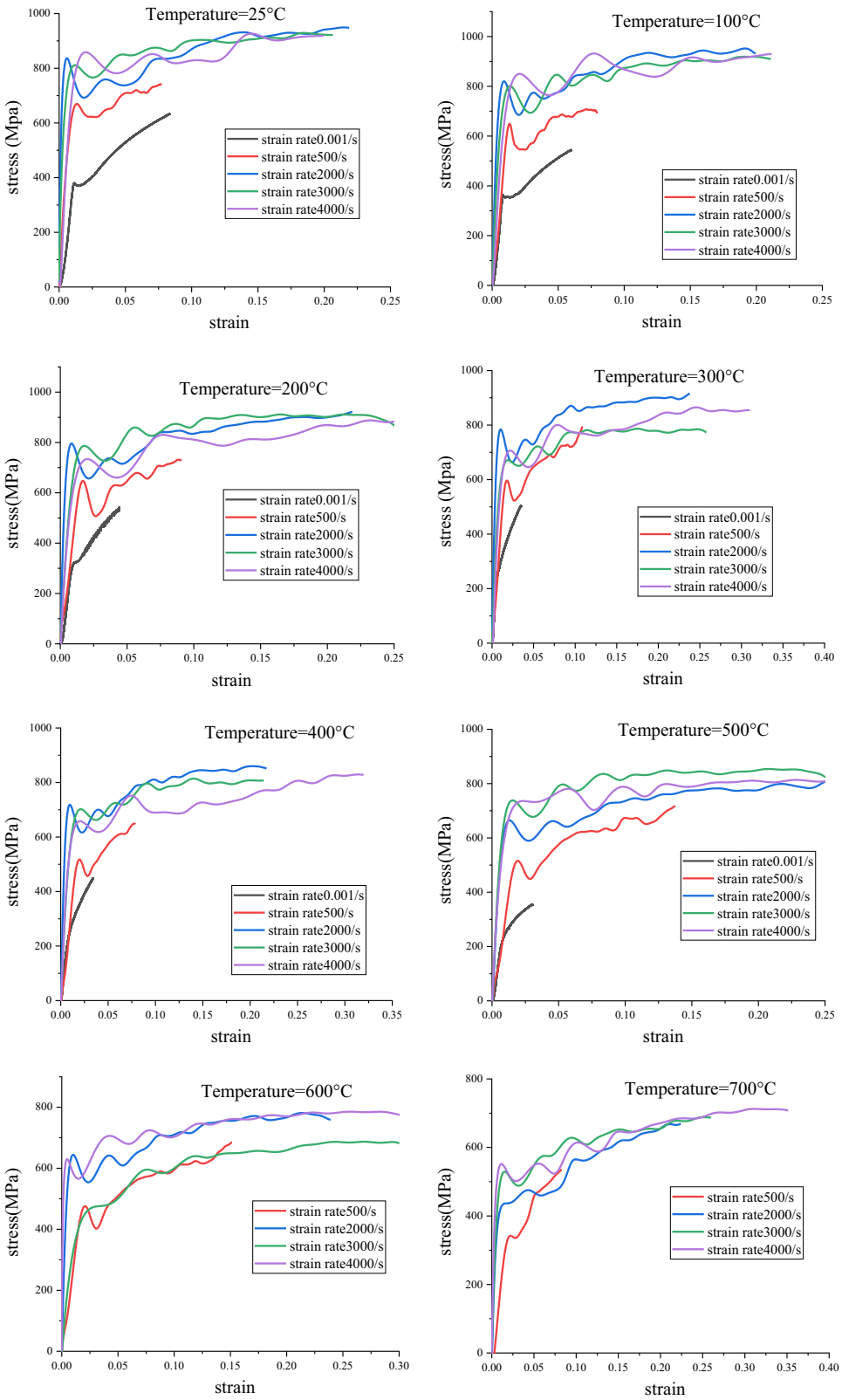

Fig. 12 True stress–strain curves for different strain rates at various temperatures

$$\sigma = (A + B\varepsilon^{\mathrm{n}})(1 + C\ln\dot{\varepsilon}^{*})\left\{1 - \left[\frac{\left[T + K(1 + C\ln\dot{\varepsilon}^{*})(1 - T^{*m})\left(A\varepsilon + B\frac{\varepsilon^{n+1}}{n+1}\right) - T_{\mathrm{r}}\right]}{T_{\mathrm{m}} - T_{\mathrm{r}}}\right]^{m}\right\}. \tag{12}$$

When the stress unit is MPa, K is 0.277.

The modified J–C model according to Eq. (12) is compared with the experimental curve (the curve at the strain rate of 2000 s^{-1}, where the strain rate of 4000 s^{-1} is taken as an example, as shown in Fig. 15. In contrast, it was identified that the accuracy of the modified calculation was limited. By rigorous analysis, the difference between quasi-static and dynamic compression tests at relatively low temperatures may lie in the material constant C, also termed the strain-rate-hardening factor.

4.2.2 The strain-rate-hardening factor *C*

By calculation, the C calculated at a range of strain rates is found to be different. The varying trend of constant C with the strain rate is illustrated in Fig. 16. The figure indicates the relation between C and strain rate (strain rate is a quadratic function overall). Thus, C can be modified as the quadratic function equation of strain rate as

$$C = C_1\dot{\varepsilon}^2 + C_2\dot{\varepsilon} + C_3. \tag{13}$$

After fitting, the specific functional relationship is expressed as

$$C = -2.52052 * 10^{-9}\dot{\varepsilon}^2 + 1.29646 * 10^{-5}\dot{\varepsilon} + 0.02826. \tag{14}$$

Further modified J–C model can be obtained by substituting the modified C into Eq. (12). Comparisons between the experimental results and modified J–C constitutive equation are drawn in Fig. 17. The modified J–C constitutive equation exhibited more prominent accuracy to express the experimental results. Thus, the J–C constitutive equation of Q345B steel after the final revision is written as

$$\begin{cases} \sigma_1 = (370 + 405\varepsilon^{0.374})(1 + 0.065\ln\dot{\varepsilon}^{*})(1 - T^{*1.02}) \\ \sigma_2 = (370 + 405\varepsilon^{0.374})(1 + C\ln\dot{\varepsilon}^{*})\left\{1 - \left[\frac{\left[T + 0.277(1 + C\ln\dot{\varepsilon}^{*})\left(1 - T^{*1.02}\right)(370\varepsilon + 294.76\varepsilon^{1.374}) - T_{\mathrm{r}}\right]}{T_{\mathrm{m}} - T_{\mathrm{r}}}\right]^{1.02}\right\} \end{cases}, \tag{15}$$

where σ_1 applies to quasi-static conditions and σ_2 applies to dynamic strain rate. C is determined by Eq. (14).

Due to the properties of the material, test methods, and other factors, only the approximate range of stress under a certain temperature and strain rate was predicted. Figure 14a suggests that the temperature sensitivity of Q345B steel significantly rises under quasi-static conditions. Figure 17 also shows that under the condition of dynamic strain rate, with the gradual increase in strain rate, the modified J–C model curve is lower than that of the experimental ones at higher temperatures. A possible explanation is that the accuracy of the J–C model declined with the increase in strain rate and temperature [42].

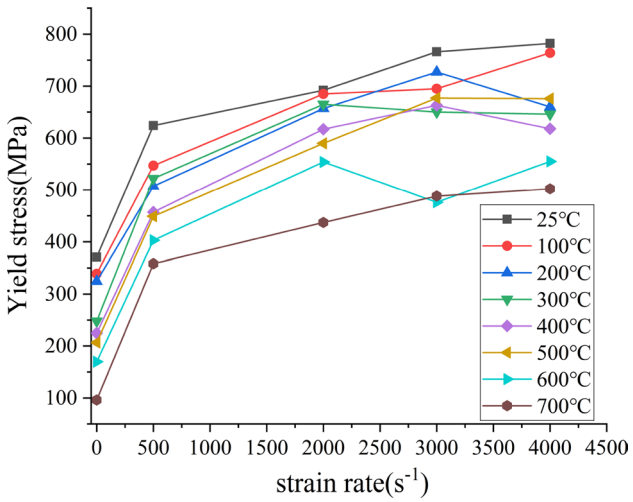

Fig. 13 Yield stress–strain-rate curve at different temperatures

Table 6 Five material constants of Q345B steel

A (MPa)	*B* (MPa)	*n*	*C*	*m*
370	405	0.374	0.065	1.02

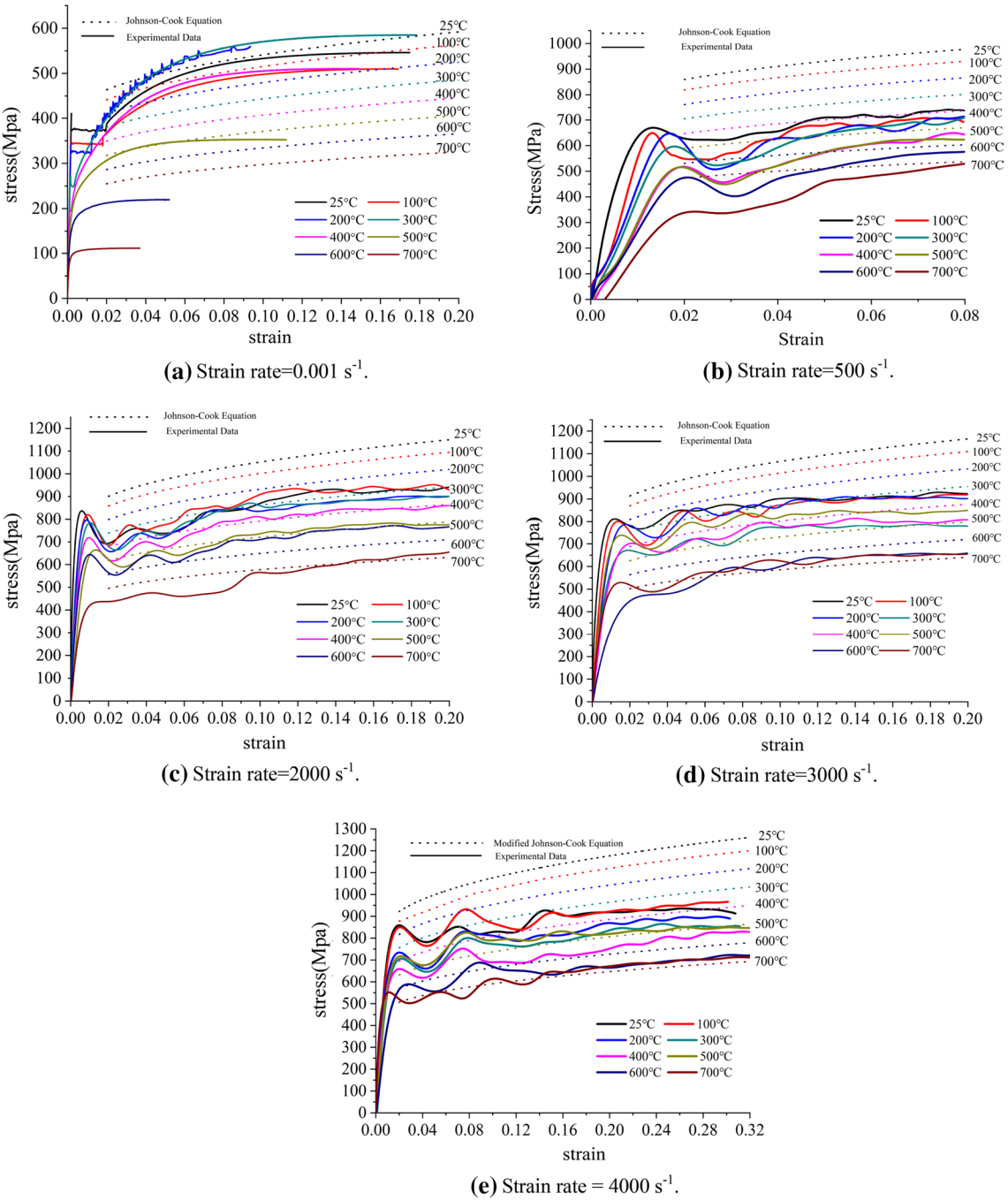

(a) Strain rate=0.001 s^{-1}.

(b) Strain rate=500 s^{-1}.

(c) Strain rate=2000 s^{-1}.

(d) Strain rate=3000 s^{-1}.

(e) Strain rate = 4000 s^{-1}.

Fig. 14 Comparison of the stress–strain curves between the J–C model and the experimental data. **a** Strain rate = 0.001 s^{-1}. **b** Strain rate = 500 s^{-1}. **c** Strain rate = 2000 s^{-1}. **d** Strain rate = 3000 s^{-1}. **e** Strain rate = 4000 s^{-1}

Table 7 Adiabatic temperature rise at different experimental temperatures under strain rates 2000 s^{-1} and 4000 s^{-1}

Experimental temperature (°C)		25	100	200	300	400	500	600	700
Adiabatic temperature rise (°C)	(2000 s^{-1})	46.71	47.51	45.11	45.18	42.49	38.86	38.02	29.45
	(4000 s^{-1})	73.7	72.9	67.52	66.69	64.04	70.04	57.56	61.42

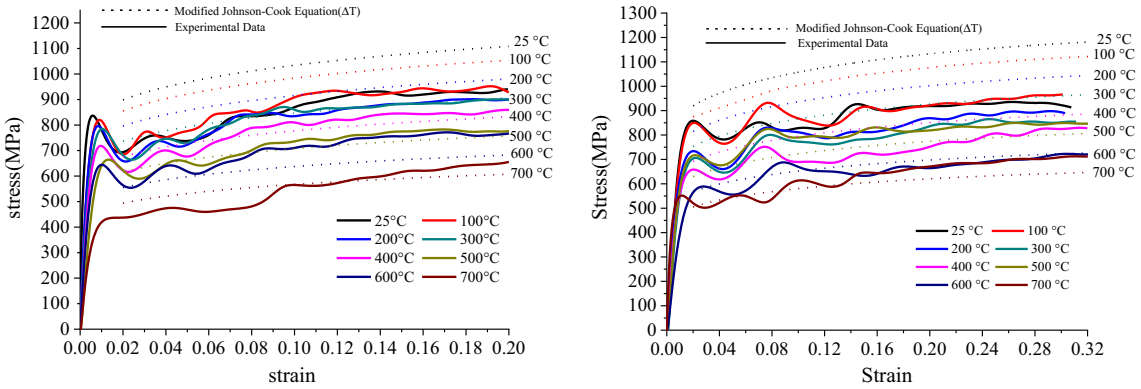

(a) 2000/s. **(b)** 4000/s.

Fig. 15 Comparison of experimental results and J–C model including the adiabatic temperature rise effect. **a** 2000 s^{-1}. **b** 4000 s^{-1}

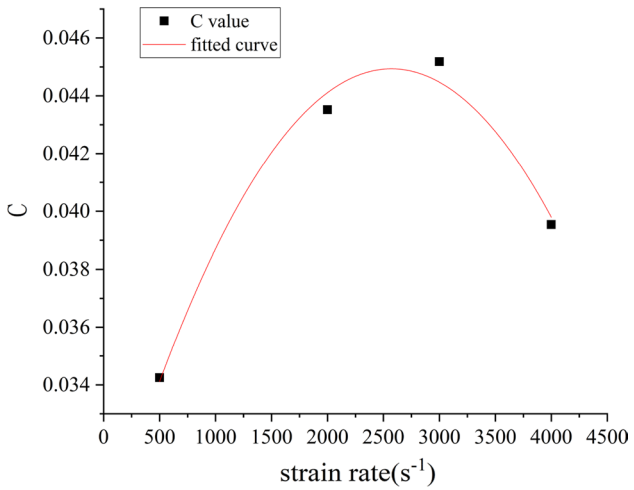

Fig. 16 Change in material constant C due to strain rate

5 Conclusion

The dynamic mechanical behavior of Q345B steel at strain rates ranging from quasi-static to 4000 s^{-1} and the temperatures (25–700 °C) was ascertained by quasi-static tensile tests and SHPB tests. The detailed findings of this study are as follows:

1. First, as revealed from the stress–strain data curves at different temperatures, Q345B steel has an obvious thermal softening effect under quasi-static and dynamic strain rates. However, due to the phenomenon of "blue brittle," the material strength increases with the rise in temperature in a certain temperature range.
2. The stress–strain curves under different strain rates show that Q345B steel has an obvious strain-rate-hardening effect within the strain rate range of 2000 s^{-1}. When the strain rate exceeds 2000 s^{-1}, Q345B steel becomes insensitive to the change in strain rate, and a strain-rate-softening effect might occur.
3. Yield strength, tensile strength, and elastic modulus as a function of temperature under quasi-static conditions were established. This can accurately describe the relationship between the three mechanical performance indexes and temperature.
4. A correction of material constant *C* made the modified J–C constitutive equation more suitable for expressing the dynamic behavior of Q345B steel.

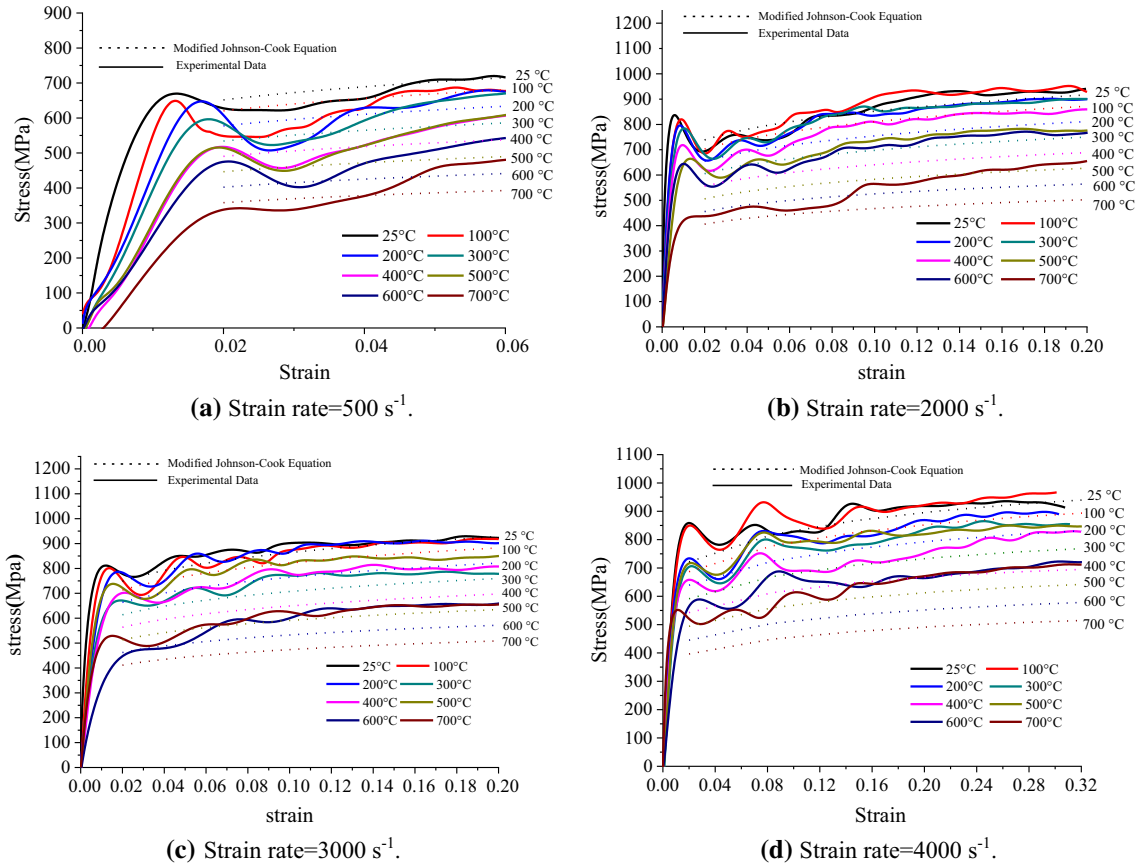

(a) Strain rate=500 s^{-1}. **(b)** Strain rate=2000 s^{-1}.

(c) Strain rate=3000 s^{-1}. **(d)** Strain rate=4000 s^{-1}.

Fig. 17 Comparison between experimental results and modified J–C constitutive equation after the correction of parameter *C*. **a** Strain rate = 500 s^{-1}. **b** Strain rate = 2000 s^{-1}. **c** Strain rate = 3000 s^{-1}. **d** Strain rate = 4000 s^{-1}

Acknowledgements The financial support from the National Natural Science Foundation of China (Grant No. 51678567) is gratefully acknowledged.

Compliance with ethical standards

Conflict of interest The authors declare that they have no conflict of interest.

References

1. Liew JY (2008) Survivability of steel frame structures subject to blast and fire. J Constr Steel Res 64(7–8):854–866
2. Arablouei A, Kodur V (2016) Modeling delamination of fire insulation from steel structures subjected to blast loading. Eng Struct 116:56–69
3. Song K, Long Y, Ji C et al (2016) Experimental and numerical studies on the deformation and tearing of X70 pipelines subjected to localized blast loading. Thin-Walled Struct 107:156–168
4. Choi SJ, Lee SW, Kim JHJ (2017) Impact or blast induced fire simulation of bi-directional PSC panel considering concrete confinement and spalling effect. Eng Struct 149:113–130
5. Xiang Z, Huo J, Wang H et al (2020) Dynamic tensile behavior of steel HRB500E reinforcing bar at low, medium, and high strain rates. Materials 13(1):185
6. Field JE, Walley SM, Proud WG et al (2004) Review of experimental techniques for high rate deformation and shock studies. Int J Impact Eng 30(7):725–775
7. Khosravani MR, Weinberg K (2018) A review on split Hopkinson bar experiments on the dynamic characterisation of concrete. Constr Build Mater 190:1264–1283
8. Sudheera RammohanYS, Pradeep MS (2018) Split Hopkinson pressure bar apparatus for compression testing: a review. Mater Today Proc 5(1):2824–2829
9. Zhao S, Zhang Q (2019) Effect of silica fume in concrete on mechanical properties and dynamic behaviors under impact loading. Materials 12(19):3263
10. Whittington WR, Oppedal AL, Turnage SA et al (2014) Capturing the effect of temperature, strain rate, and stress state on the plasticity and fracture of rolled homogeneous armor (RHA) steel. Mater Sci Eng 594:82–88
11. Visser W, Ghonem H (2019) Dynamic flow stress of shock loaded low carbon steel. Mater Sci Eng A 753:317–330
12. Jing L, Xingya S, Zhao L (2017) The dynamic compressive behavior and constitutive modeling of D1 railway wheel steel over a wide range of strain rates and temperatures. Res Phys 7:1452–1461

13. Li X, Roth CC, Mohr D (2019) Machine-learning based temperature-and rate-dependent plasticity model: application to analysis of fracture experiments on DP steel. Int J Plast 118:320–344
14. Niu Q, Ming W, Chen M et al (2017) Dynamic mechanical behavior of ultra-high strength steel 30CrMnSiNi2A at high strain rates and elevated temperatures. J Iron Steel Res Int 24(7):724–729
15. Lee WS, Liu C (2006) The effects of temperature and strain rate on the dynamic flow behaviour of different steels. Mater Sci Eng 426(1–2):101–113
16. Iqbal MA, Senthil K, Sharma P et al (2016) An investigation of the constitutive behavior of Armox 500T steel and armor piercing incendiary projectile material. Int J Impact Eng 96:146–164
17. Erice B, Galvez F, Cendon DA et al (2012) Flow and fracture behaviour of FV535 steel at different triaxialities, strain rates and temperatures. Eng Fract Mech 79:1–17
18. Brown LB, Hazell PJ, Crouch IG et al (2017) Computational and split-Hopkinson pressure-bar studies on the effect of the jacket during penetration of an AK47 bullet into ceramic armor. Mater Des 119:47–53
19. Seo S, Min O, Yang H (2005) Constitutive equation for Ti–6Al–4V at high temperatures measured using the SHPB technique. Int J Impact Eng 31(6):735–754
20. Pao YH, Gilat A (1992) High strain rate deformation and failure of A533B steel at various temperatures. Acta Metall Mater 40(6):1271–1280
21. Zhu Z, Yesen L, Xie Q et al (2017) Mechanical properties and dynamic constitutive model of 42CrMo steel. Mater Des 119:171–179
22. Li D, Wei Y, Liu C et al (2010) Effects of high strain rate on properties and microstructure evolution of TWIP steel subjected to impact loading. J Iron Steel Res Int 17(6):67–73
23. Zejian X, Huang F (2012) Plastic behavior and constitutive modeling of armor steel over wide temperature and strain rate ranges. Acta Mech Solida Sin 25(6):598–608
24. Tasdemirci A, Ergoenenc C, Gueden M (2010) Split Hopkinson pressure bar multiple reloading and modeling of a 316L stainless steel metallic hollow sphere structure. Int J Impact Eng 37(3):250–259
25. Lee W-S, Lin C, Chen T et al (2012) High temperature deformation and fracture behaviour of 316L stainless steel under high strain rate loading. J Nucl Mater 420(1–3):226–234
26. Quinlan MF, Hillery MT (2004) High-strain-rate testing of beryllium copper at elevated temperatures. J Mater Process Technol 153:1051–1057
27. Khan AS, Kazmi R, Farrokh B et al (2007) Effect of oxygen content and microstructure on the thermo-mechanical response of three Ti–6Al–4V alloys: experiments and modeling over a wide range of strain-rates and temperatures. Int J Plast 23(7):1105–1125
28. Zhang J, Wang Y, Zan X et al (2015) The constitutive responses of Ti–6.6Al–3.3Mo–1.8Zr–0.29 Si alloy at high strain rates and elevated temperatures. J Alloys Compd 647:97–104
29. Lee OS, Choi H, Kim H (2011) High-temperature dynamic deformation of aluminum alloys using SHPB. J Mech Sci Technol 25:143–148
30. Bobbili R, Ramakrishna B, Madhu V et al (2015) Prediction of flow stress of 7017 aluminium alloy under high strain rate compression at elevated temperatures. Def Technol 11(1):93–98
31. Vilamosa V, Clausen AH, Borvik T et al (2015) Behaviour of Al–Mg–Si alloys at a wide range of temperatures and strain rates. Int J Impact Eng 86:223–239
32. GB/T 228.1-2010 (2010) Metallic materials tensile testing—part 1: method of test at room temperature. China Standard
33. GB/T 228.2-2015 (2015) Metallic materials tensile testing—part 2: method of test at elevated temperature. China Standard
34. GB/T 7314-2017 (2017) Metallic materials-compression test method at room temperature. China Standard
35. Xu Z, Liu Y, Hu H, et al (2019) Determination of shear behavior and constitutive modeling of the 603 steel over wide temperature and strain rate ranges. J Mech Phys Solids 129:184–204
36. Yu W (2012) Study on mechanical properties of steel structure of jacket offshore platform under explosion and fire. Shanghai Jiao Tong Univ 31–33
37. Peng R (2017) Mechanical properties of materials. China Machine Press, Beijing, pp 17–18
38. Johnson GR, Cook WH (1985) Fracture characteristics of three metals subjected to various strains, strain rates, temperatures and pressures. Eng Fract Mech 21(1):31–48
39. Mason JJ, Rosakis AJ, Ravichandran G (1994) On the strain and strain rate dependence of the fraction of plastic work converted to heat: an experimental study using high speed infrared detectors and the Kolsky bar. Mech Mater 17(2–3):135–145
40. Xiangyu W, Chuanzhen H, Bin Z et al (2013) Dynamic behavior and a modified Johnson–Cook constitutive model of Inconel 718 at high strain rate and elevated temperature. Mater Sci Eng A 580:385–390
41. Sun J, Guo YB (2009) Material flow stress and failure in multiscale machining titanium alloy Ti–6Al–4V. Int J Adv Manuf Technol 41(7–8):651–659
42. Zhou L, Zihao WANG, Wen H (2019) On the accuracy of the Johnson–Cook constitutive model for metals. Chin J High Pressure Phys 33(4):3–16